

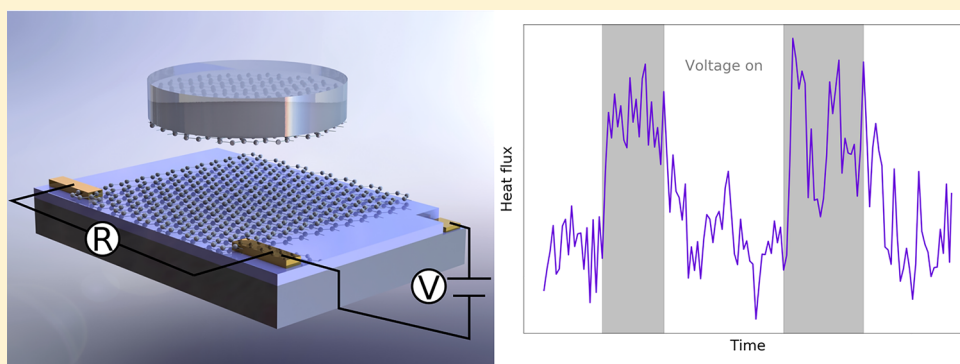
Electronic Modulation of Near-Field Radiative Transfer in Graphene Field Effect Heterostructures

Nathan H. Thomas,[†] Michelle C. Sherrott,^{‡,¶} Jeremy Broulliet,[‡] Harry A. Atwater,^{†,‡} and Austin J. Minnich^{*,†}

[†]Division of Engineering and Applied Science, California Institute of Technology, Pasadena, California 91125, United States

[‡]Thomas J. Watson Laboratory of Applied Physics, California Institute of Technology, Pasadena, California 91125, United States

S Supporting Information



ABSTRACT: Manipulating heat flow in a controllable and reversible manner is a topic of fundamental and practical interest. Numerous approaches to perform thermal switching have been reported, but they typically suffer from various limitations, for instance requiring mechanical modulation of a submicron gap spacing or only operating in a narrow temperature window. Here, we report the experimental modulation of radiative heat flow by electronic gating of a graphene field effect heterostructure without any moving elements. We measure a maximum heat flux modulation of $4 \pm 3\%$ and an absolute modulation depth of $24 \pm 7 \text{ mW m}^{-2} \text{ V}^{-1}$ in samples with vacuum gap distances ranging from 1 to 3 μm . The active area in the samples through which heat is transferred is $\sim 1 \text{ cm}^2$, indicating the scalable nature of these structures. A clear experimental path exists to realize switching ratios as large as 100%, laying the foundation for electronic control of near-field thermal radiation using 2D materials.

KEYWORDS: Near-field radiative transfer; graphene; electronic modulation; thermal switches

Thermal switches that change thermal resistance in response to external stimuli have long been desired for temperature control applications.¹ Typical thermal switches used in practice operate by mechanical mechanisms such as changing the physical contact of metallic leads, which are prone to failure.² Numerous other schemes for controlling conductive heat flow have been proposed, including biasing of ferroelectrics,^{3–5} exploiting changes in properties across a phase transition,^{6–9} and magnetically aligning crystal networks.¹⁰ Thermal switches for radiative heat transfer can be realized if the optical dielectric constant or optical resonances at a surface can be altered by an external stimulus.^{11–14} In particular, theoretical and experimental works have described radiative heat flux modulation based on the insulator–metal transition of VO_2 .^{15–18}

Two-dimensional materials offer the capability to alter the surface dielectric function by electronic tuning of the free carrier concentration in a fast, controllable, and reversible manner without restrictions in operating temperature.^{19–25} Despite this capability, achieving even modest modulation of far-field radiative flux is challenging as thermal radiation is

broadband. In the near-field, however, thermal radiation is primarily due to resonant coupling of narrowband surface modes, such as plasmons or phonon polaritons.^{26,27} Additionally, near-field radiative flux can be orders of magnitude larger than the far-field blackbody limit, and thus near-field radiative heat transport has been an area of intense experimental^{28–37} and theoretical^{38–46} interest.

Graphene has been proposed as an ideal material for thermal switching of near-field radiation as it exhibits a plasmonic resonance in the mid-infrared that can be electronically modulated.^{47–51} Recent experimental works have reported that graphene enables enhanced radiative thermal coupling between polar materials in the near-field.^{52,53} However, these studies do not take advantage of the electronic tunability of graphene to modulate heat flow. Recently, a theoretical scheme was proposed to electronically control radiative flow in a graphene field effect device, but an experimental implementa-

Received: March 15, 2019

Revised: May 10, 2019

Published: May 29, 2019

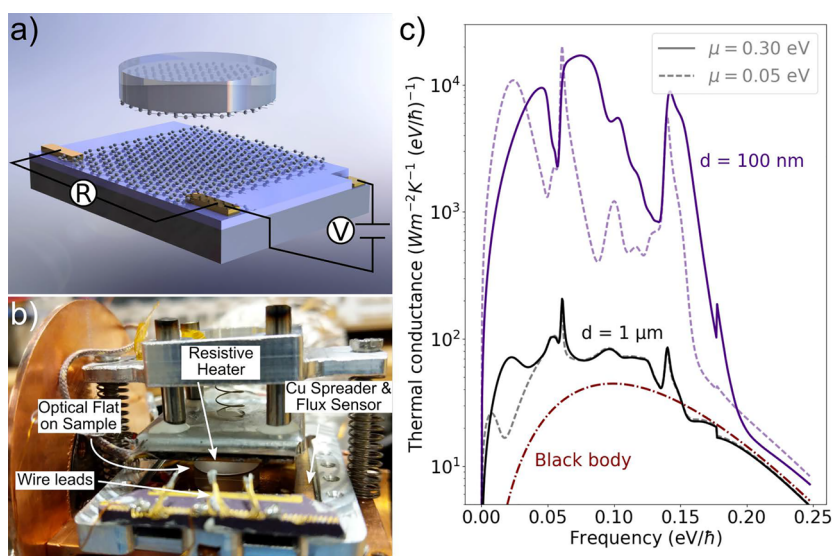


Figure 1. Experimental approach to measure near-field heat flux modulation. (a) Schematic of sample configuration. The top of the heterostructure is an optical flat, coated with graphene. The bottom is a graphene-coated silicon wafer (gray) with 285 nm of thermally grown SiO₂ and 8 nm of ALD Al₂O₃ (purple). The graphene sheets are assumed to have the same Fermi level due to physical contact of the top and bottom. (b) Image of the experimental stage with mounted sample. (c) Calculated spectral thermal conductance at 300 K with a vacuum gap spacing of 100 nm (purple lines) and 1 μm (black lines). The Fermi levels range from 0.05 eV (dotted lines) to 0.3 eV (solid lines), which are chosen as conservative estimates for the lower and upper magnitudes achievable for graphene with a charge neutral point near 0 V and a maximum applied voltage of ± 100 V. The three sharp spectral features at frequencies above 0.06 eV originates from the phonon-polariton resonances in the SiO₂.⁶⁰ The broad feature at frequencies below 0.06 eV originates from the graphene plasmon.

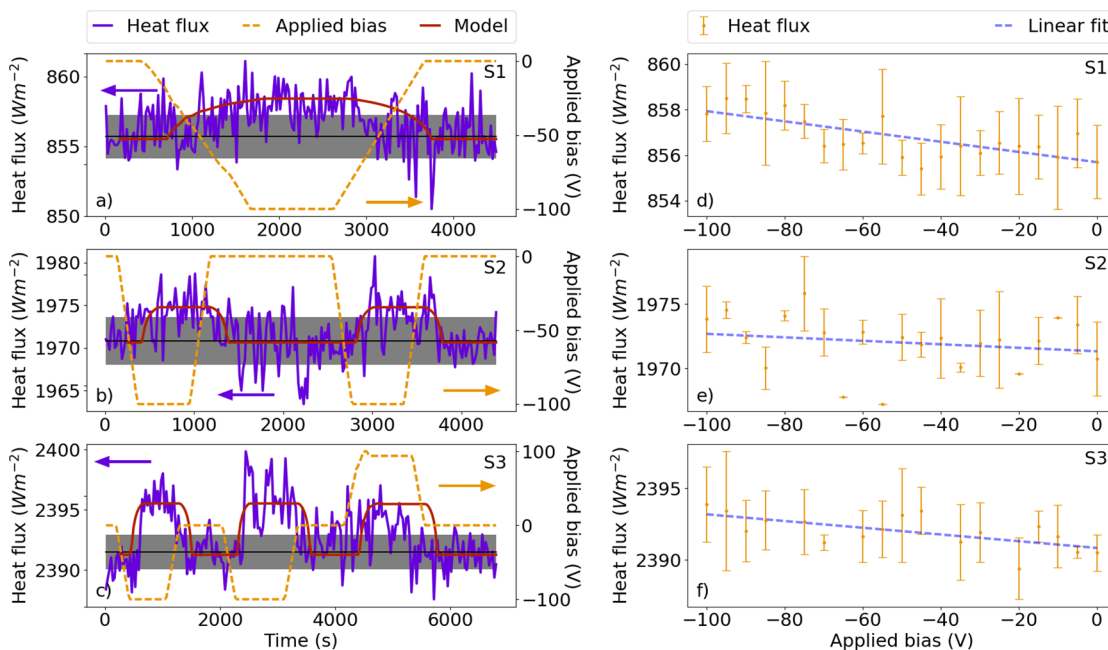


Figure 2. Heat flux modulation and modulation depth. (a)–(c) Heat flux (purple), applied bias (orange dotted), and thermal model (red) versus time for three samples S1, S2, and S3, respectively. The black and gray lines indicate the mean and standard deviation of the signal at zero bias. (d)–(f) Heat flux versus applied bias using data from Figure 2a–c. The linear fit (blue dotted lines) indicate the greatest heat flux modulation occurs for S3, for which the modulation is $24 \pm 7 \text{ mW m}^{-2} \text{ V}^{-1}$.

tion of a radiative thermal switch based on such a device has not yet been reported.⁵⁴

We implemented an experiment to demonstrate such a thermal switch using a graphene heterostructure device. As shown schematically in Figure 1a, the top of the device is a graphene-coated silica optical flat, and the bottom is a back-gated, graphene-coated silicon wafer with a gate dielectric of 285 nm of SiO₂ and 8 nm of Al₂O₃. An image of the sample on

the experimental stage is shown in Figure 1b. The spring-loaded resistive heater presses the optical flat to the silicon wafer, which rests on a copper heat spreader with an embedded heat flux sensor (see Methods and the Supporting Information, Section 1).

We apply a standard fluctuational electrodynamics formalism^{55–57} to assess the potential for this sample configuration to modulate near-field radiative flow. In Figure 1c, we present

calculations of the spectral thermal conductance, defined as $h(\omega) = \partial Q(\omega)/\partial T$, where Q is the radiative heat flux, for our device at $T = 300$ K at various gap distances and Fermi levels. A clear change in spectral heat flux with Fermi level is evident. At vacuum gaps up to around 500 nm, the hybrid phonon-plasmon-polariton can be tuned with the graphene Fermi level.^{54,58,59} However, this mode is tightly confined to the surface and does not contribute to heat flow at gap distances exceeding 1 μm . As a result, in the present experiments, where the vacuum separation distances between the top and bottom exceed 1 μm , the heat flux modulation originates only from the nonhybridized graphene plasmon. The spectral features from the SiO_2 only contribute to the background heat flux.⁵⁴ We obtain the total thermal conductance h by integrating over all frequencies and define a thermal switching figure of merit as the ratio $h(\mu = 0.3 \text{ eV})/h(\mu = 0.05 \text{ eV})$. This ratio is 2.1 at $d = 100$ nm for a total heat flux change over 100%. At $d = 1 \mu\text{m}$ the ratio is 1.1, indicating a strong vacuum gap dependence on the influence of external bias to heat flux. Although at gap distances exceeding 1 μm the optically active dielectric and substrate decrease the switching ratio, modulation should be observable with this experimentally achievable configuration.

The experiments are conducted in a cryostat cooled to 77 K, where a resistive heater is used to heat the top of the sample. Once the temperatures equilibrate, the heat flux is monitored while a voltage ramp is applied to the back-gated bottom of the heterostructure via wire-bonded Au contacts (see [Methods](#)). Parts a–c of [Figure 2](#) show the measured heat flux versus time for three separate samples S1, S2, and S3. The steady-state temperatures T_1 and T_2 for each sample are 197 and 86 K for S1 and 270 and 91 K for S2 and 269 and 90 K for S3, respectively. For each sample, we observe a reversible change in the measured heat flux as the bias is ramped up and down. The magnitude of the modulation is around 0.5%, 0.3%, and 0.2%, respectively. For samples S2 and S3, this effect is observed for multiple cycles. As a non-negligible thermal capacitance exists, there is a time delay from when the bias is applied and when the heat flux change is observed. For each sample, this delay was about 3 min. All samples were first ramped down to -100 V, which resulted in an observable change in heat flux. For S2, the bias could be ramped twice before sample failure. For S3, three cycles were possible, and the third ramp cycle was to a positive bias of +95 V.

A similar magnitude of heat flux change is observed for positive biases as negative biases. This result is expected because the graphene is slightly p-type with the charge neutral point found to be slightly positive, between +5 and +15 V. As a negative bias is applied, the hole concentration increases, the Fermi level becomes more negative, and the radiative thermal conductance increases. Applying a positive bias of +95 V versus a negative bias of -100 V results in a Fermi level of 0.29 eV instead of -0.32 eV, which is not sufficiently different in magnitude for a measurable change in heat flux considering the noise in the measurement.

From these data, we compute the heat flux versus electronic bias, shown in in [Figure 2d–f](#) for samples S1–S3, respectively. In each case, a linear fit is applied and a modest slope is visible, with the largest modulation exhibited in S3 with a slope of $24 \pm 7 \text{ mW m}^{-2} \text{ V}^{-1}$.

We now examine the origin of this signal. First we rule out Joule heating by ensuring that the leakage current does not exceed 350 nA for these three samples, limiting parasitic Joule heating to a maximum of 0.26 W m^{-2} . The observed heat flux

change is on the order of 5 W m^{-2} in all cases, or nearly 20 times higher. For each measurement, we subtract the area normalized injected power $P = IV$. We also confirm independently that the injected Joule heat is not the cause of the modulated signal. For S3, the leakage power is approximately 20 times higher during the final voltage cycle than in the two previous cycles (see the [Supporting Information](#), Section 6). If Joule heating were the source of the heat flux change, then in the final cycle the heat flux change would be 20 \times higher than in the previous cycles. As shown in [Figure 2c](#), the change is nearly identical.

Next, we construct a thermal model. The heat flux measured in the experiment as a function of time consists of radiative flux and parasitic conductive losses:

$$Q_{\text{tot}}(t - \tau) = G(T_1 - T_2) + Q_{\text{rad}}(\mu(t), d, T_1, T_2) \quad (1)$$

The first term accounts for the physical contact of the top and bottom surfaces with a conductance G . The second term, $Q_{\text{rad},d}$, is the radiative heat flux between the planar surfaces.^{30,56,61} In the model, the temperatures are fixed and the radiative thermal conductance changes due to the changing Fermi level. The time dependence in the heat flux is accounted for in the time-dependent nature of the voltage ramp and phenomenologically in the adjustable time delay τ between the start of the voltage ramp and when the heat flux sensor registers the flux change. Since the top and bottom are likely in physical contact, it is assumed that the two graphene sheets are shorted such that $\mu_1 = \mu_2 = \mu$. The values for μ , T_1 , and T_2 are measured in the experiment (See [Methods](#) and the [Supporting Information](#), Section 6). We use optical interferometric measurements to estimate the effective gap distance d , and separate measurements without spacers to estimate the value of the parasitic conductance G . The final values for d and G for each sample are obtained in two independent fitting procedures, using the measured heat flux change and the calculated radiative flux (see the [Supporting Information](#), Section 6).

The model predictions are plotted in [Figures 2a–c](#) and agree well with the measured heat flux. For samples S1–S3, the fitted values for G are 6.6 ± 0.2 , 8.9 ± 0.2 , and $11.3 \pm 0.2 \text{ W m}^{-2} \text{ K}^{-1}$, respectively, and for d are 2.5 ± 0.2 , 2.3 ± 0.2 , and $2.3 \pm 0.13 \mu\text{m}$, respectively. These values indicate non-negligible physical contact between the optical flat and the bottom substrate and also a vacuum gap, commensurate with previous near-field heat transfer experiments.²⁸ After the initial time delay, the heat flux increases to its steady-state value and then decreases to the equilibrium value, following the measured heat flux. During the final, third voltage ramp for S3, there is a slight deviation from the model at later stages when the peak voltage of +95 V was applied. We attribute this discrepancy to the sample dielectric beginning to break down, decreasing the electric field effect and subsequently lowering the Fermi level compared to that used in the model.

With the model and the fitted gap distances, we can also estimate the absolute radiative heat flux between the two surfaces. Subtracting the conductive contribution, we find the radiative heat flux for S1 is $125 \pm 9 \text{ W m}^{-2}$, exceeding the blackbody limit of $84 \pm 4 \text{ W m}^{-2}$ by $50 \pm 10\%$. For samples S2 and S3, the thermal emitter is approximately 80 K hotter than for S1, and the radiative heat flux is 385 ± 26 and $381 \pm 18 \text{ W m}^{-2}$ for S2 and S3, respectively. Sample S2 exceeds the blackbody limit of $299 \pm 9 \text{ W m}^{-2}$ by $29 \pm 7\%$, and sample S3 exceeds the blackbody limit of $295 \pm 9 \text{ W m}^{-2}$ by $29 \pm 9\%$.

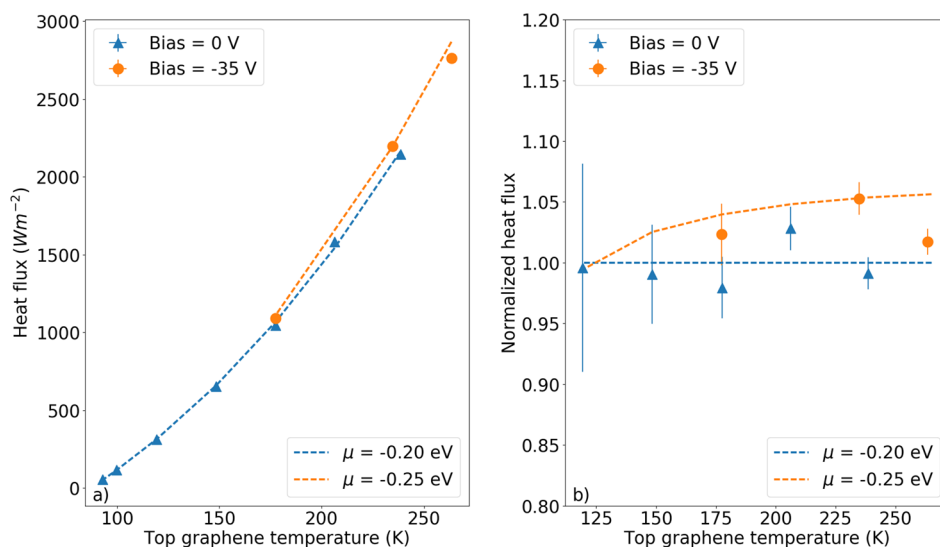


Figure 3. Heat flux versus temperature at different voltages. (a) Measured heat flux versus temperature for sample S4 for 0 V (blue triangles) and -35 V (orange circles). The blue dotted line is a fit of eq 1 to the blue data points, for which $d = 560$ nm, $G = 5.07$ W m⁻² K⁻¹, and $\mu = -0.20$ eV. The orange line is a zero parameter fit, using these values and a Fermi level of $\mu = -0.25$ eV corresponding to the -35 V bias. (b) Normalized heat flux versus temperature for the two biases. The heat flux under bias is greater than the zero bias case by around 3–5%.

These results confirm that the radiative transport is in the near-field regime (see Supporting Information, Section 7).

We next present the heat flux versus hot side temperature for sample S4 for two different biases, as shown in Figure 3a. The heat flux is first measured at zero bias and then at -35 V. Additional measurements at temperatures below the third point at 175 K were not possible due to dielectric breakdown. We again interpret these results using the model described previously, where here we fit for G , d , and μ (see the Supporting Information, Section 6). Using the fitting parameters from the zero bias data, we then apply a zero-parameter fit for the measurement under bias, accounting for the change in Fermi level. The model shows good agreement with the measured heat flux.

In Figure 3b, the data are normalized to the dotted blue fit. Point to point variation in both signals is evident, but there is also a clear trend that heat flux in the biased case is greater than that in the zero bias case by around 3–5%. At 175 K, where both the biased and zero bias case were measured and a more direct comparison is possible, the heat flux change is $4 \pm 3\%$.

Although the modulation reported here is of the order of a few percent, as expected due to the micron-scale gap spacing, improvements to the experimental setup should allow for modulation values approaching 100%. Primarily, the gate dielectric must exhibit high breakdown strength approaching that of bulk SiO₂ while also exhibiting warping less than 100 nm over the substrate area. These qualities would allow for larger biases, small vacuum gaps, and reduced conductive contact. By eliminating all conductive losses and reducing the gap spacing to 100 nm, biasing to -100 V as in these experiments would result in a heat flux modulation of 100%. Reducing the gap distance to such a value would also allow for coupling between the graphene plasmon and the phonon polariton in the dielectric to influence heat flow.⁵⁴ However, even reducing the gap to 500 nm without any change in the interface conductance would lead to modulation of 45%.

In summary, we report the experimental demonstration of the modulation of near-field thermal radiation by electronic

gating of 1 cm² scale graphene heterostructures. The maximum measured modulation was $4 \pm 3\%$, and the maximum measured modulation depth was 24 ± 7 mW m⁻² V⁻¹. This work demonstrates that two-dimensional materials can be used to electronically control near-field radiative transfer and provides a path for realizing thermal switches with modulation depth approaching 100%.

Methods. Sample Fabrication. The bottom substrate is a silicon wafer with a thermally grown oxide of 285 nm thickness. On its own, the thermally grown SiO₂ is not adequate for biasing to large voltages of ~ 100 V, and an extra 8 nm layer of Al₂O₃ was deposited using atomic layer deposition to increase breakdown strength. The wafers are cleaved to pieces 25.4 mm \times 31.75 mm and are cleaned in isopropyl alcohol in a sonicator, followed by an O₂ plasma clean and an overnight soak in Piranha solution. [Caution: Piranha solution is aggressive and explosive. Never mix piranha waste with solvents. Check the safety precautions before using it.] Graphene pieces 15 mm \times 20 mm are transferred to the substrate by a modified wet transfer technique (see the Supporting Information, Section 2). The top substrate is an optical flat, 12.7 mm in diameter, which is cleaned and has graphene transferred to it in an identical manner. Gold bonding contacts and the array of SiO₂ posts, each 1 μ m square and spaced 500 μ m apart, are fabricated on the bottom substrate by electron beam lithography and subsequent electron beam evaporation. Of the four different samples studied here, the pillars are grown to 200 nm tall for samples S1, S2, and S4, and 400 nm tall for sample S3.

Experimental Protocol. After fabrication, the optical flat is pressed down onto the bottom substrate by a spring loaded resistive heater, shown in Figure 1c. Beneath the sample is a thermopile heat flux sensor, which has been calibrated at temperatures from 90 to 300 K by measuring the output signal as a function of input power into a resistive heater (see the Supporting Information, Section 3). A copper heat spreader is secured to the top of the sensor with thermally conductive epoxy. The entire array sits on a copper base that is screwed to the coldfinger of a cryostat that is pumped down to 1×10^{-6}

Torr during the experiment. The external bias is applied through wire bonded gold pads on the sample. The temperatures of the coldfinger and heater are measured with a Si-diode and a K-type thermocouple, respectively, and are maintained through two independent PID controllers. The copper base and the heat flux sensor temperatures are measured by K-type thermocouples, and the graphene surface resistance is recorded with a Fluke multimeter while the sample is biased with a Keithley 2410 source meter.

The coldfinger is cooled to 77 K with a liquid nitrogen feed and the resistive heater is set to a maximum input power. The equilibrium temperature of the heterostructure bottom reaches between 86 and 91 K, but the maximum temperature of the resistive heater is dependent on the nitrogen flow rate. For sample S1, the top temperature reaches 197 K. For samples S2 and S3, the top temperature reaches 269 K and 270 K, respectively. For the measurements of heat flux over time, after the heat flux sensor has equilibrated, the sample voltage is applied at a constant ramp rate. It was found that equilibration can take several hours, so there is a linear drift in the heat flux signal that is corrected (see the [Supporting Information](#), Section 4). The ramp rate varies from sample to sample as the quality of the gate dielectric varies for each sample. The leakier the gate dielectric, the slower the ramp. The fastest ramp was 0.4 V s^{-1} for S2 and S3 and the slowest was 0.1 V s^{-1} for S1. After the voltage is held at its maximum value for around 15 min, the voltage is ramped down at the same rate.

The measurement of heat flux at different temperatures follows a similar procedure, although the two bias conditions are tracked separately. First, the heat flux was measured at different temperatures at zero bias, and then the heat flux was measured at different temperatures at -35 V . Again, the maximum heater temperature is determined by the upper limit of the heater input power. Over the course of a measurement, the liquid nitrogen flow rate falls with the pressure within the dewar. The maximum temperature is higher for the biased case over the zero-bias case because the flow rate and therefore the cooling power of the liquid nitrogen to the coldfinger was lower. For all samples tested here, we find that after a few ramping cycles the gate dielectric breaks down, limiting the amount of data that can be obtained for each sample.

Simulations and Modeling. A transfer matrix method is used to calculate the Fresnel coefficients r_1 and r_2 in the heat flux calculation for planar media,⁴⁶ with the graphene modeled as a conducting surface with a local optical conductivity.⁶² See the [Supporting Information](#), Section 9, for optical properties of SiO_2 and Al_2O_3 . The graphene conductivity was calculated at 300 K with a scattering time of $\tau = 50 \times 10^{-15} \text{ s}$, which reasonably corresponds to the quality of graphene films grown by chemical vapor deposition.⁶³

Using the measured applied voltage, we apply a capacitor model to determine the Fermi levels. To determine the temperatures of the graphene surfaces, we employ a thermal resistor model using our knowledge of the heat flux and the measured temperatures of the thermal sinks (in this case, the heater and the copper heat spreader of the heat flux sensor, see the [Supporting Information](#), Section 1).³⁶ To first approximation, we assume that the thermal resistance between top and bottom samples is much greater than that between the bottom sample and the copper heat spreader. As the bottom sample substrate is silicon, which has a comparatively high thermal conductivity, the bottom graphene surface temperature is approximately equal to that of the heat flux sensor. For

the top sample, a considerable temperature drop occurs across the optical flat, and the resistor model is necessary (see the [Supporting Information](#), Section 6).

■ ASSOCIATED CONTENT

Supporting Information

The Supporting Information is available free of charge on the [ACS Publications website](#) at DOI: [10.1021/acs.nanolett.9b01086](https://doi.org/10.1021/acs.nanolett.9b01086).

Sample schematic, graphene wet transfer technique, heat flux sensor calibration, background heat flux analysis, signal drift correction, fitting procedure for the thermal model, signal-to-noise and uncertainty, leakage current analysis, and optical properties (PDF)

■ AUTHOR INFORMATION

Corresponding Author

*E-mail: aminnich@caltech.edu.

ORCID

Nathan H. Thomas: [0000-0003-4648-5325](https://orcid.org/0000-0003-4648-5325)

Harry A. Atwater: [0000-0001-9435-0201](https://orcid.org/0000-0001-9435-0201)

Austin J. Minnich: [0000-0002-9671-9540](https://orcid.org/0000-0002-9671-9540)

Present Address

[¶]Research Laboratory of Electronics, Massachusetts Institute of Technology, Cambridge, MA 02139.

Author Contributions

N.H.T. and A.J.M. conceived and designed the experiment. N.H.T. fabricated samples and conducted numerical simulations. M.C.S. assisted in design and sample fabrication. J.B. assisted in sample fabrication. N.H.T., H.A.A., and A.J.M. wrote the manuscript. All authors commented and approved the manuscript.

Notes

The authors declare no competing financial interest.

■ ACKNOWLEDGMENTS

This work is part of the Light-Material Interactions in Energy Conversion Energy Frontier Research Center funded by the U.S. Department of Energy, Office of Science, Office of Basic Energy Sciences under Award No. DE-SC0001293. This material is based upon work supported by the National Science Foundation Graduate Research Fellowship under Grant No. 1144469. M.C.S. gratefully acknowledges fellowship support from the Resnick Sustainability Institute. The authors recognize the Kavli NanoScience Institute at Caltech and to thank Dr. Ognjen Ilic for insightful conversation.

■ REFERENCES

- (1) Wehmeyer, G.; Yabuki, T.; Monachon, C.; Wu, J.; Dames, C. Thermal diodes, regulators, and switches: Physical mechanisms and potential applications. *Appl. Phys. Rev.* **2017**, *4*, 041304.
- (2) Shu, Q. S.; Demko, J. A.; Fesmire, J. E. Heat switch technology for cryogenic thermal management. *IOP Conf. Ser.: Mater. Sci. Eng.* **2017**, *278*, 012133.
- (3) Ihlefeld, J. F.; Foley, B. M.; Scrymgeour, D. A.; Michael, J. R.; McKenzie, B. B.; Medlin, D. L.; Wallace, M.; Trolier-McKinstry, S.; Hopkins, P. E. Room-Temperature Voltage Tunable Phonon Thermal Conductivity via Reconfigurable Interfaces in Ferroelectric Thin Films. *Nano Lett.* **2015**, *15*, 1791–1795.
- (4) Foley, B. M.; Wallace, M.; Gaskins, J. T.; Paisley, E. A.; Johnson-Wilke, R. L.; Kim, J.-W.; Ryan, P. J.; Trolier-McKinstry, S.; Hopkins, P. E.; Ihlefeld, J. F. Voltage-Controlled Bistable Thermal Conductivity

in Suspended Ferroelectric Thin-Film Membranes. *ACS Appl. Mater. Interfaces* **2018**, *10*, 25493–25501.

(5) Seijas-Bellido, J. A.; Escorihuela-Sayalero, C.; Royo, M.; Ljungberg, M. P.; Wojde, J. C.; Iiguez, J.; Rurali, R. A phononic switch based on ferroelectric domain walls. *Phys. Rev. B: Condens. Matter Mater. Phys.* **2017**, *96*, 140101.

(6) Zheng, R.; Gao, J.; Wang, J.; Chen, G. Reversible temperature regulation of electrical and thermal conductivity using liquid-solid phase transitions. *Nat. Commun.* **2011**, *2*, 289.

(7) Choe, H. S.; Suh, J.; Ko, C.; Dong, K.; Lee, S.; Park, J.; Lee, Y.; Wang, K.; Wu, J. Enhancing Modulation of Thermal Conduction in Vanadium Dioxide Thin Film by Nanostructured Nanogaps. *Sci. Rep.* **2017**, *7*, 7131.

(8) Chen, R.; Cui, Y.; Tian, H.; Yao, R.; Liu, Z.; Shu, Y.; Li, C.; Yang, Y.; Ren, T.; Zhang, G.; Zou, R. Controllable Thermal Rectification Realized in Binary Phase Change Composites. *Sci. Rep.* **2015**, *5*, 8884.

(9) Kim, K.; Kaviani, M. Thermal conductivity switch: Optimal semiconductor/metal melting transition. *Phys. Rev. B: Condens. Matter Mater. Phys.* **2016**, *94*, 155203.

(10) Shin, J.; Kang, M.; Tsai, T.; Leal, C.; Braun, P. V.; Cahill, D. G. Thermally Functional Liquid Crystal Networks by Magnetic Field Driven Molecular Orientation. *ACS Macro Lett.* **2016**, *5*, 955–960.

(11) Otey, C. R.; Lau, W. T.; Fan, S. Thermal Rectification through Vacuum. *Phys. Rev. Lett.* **2010**, *104*, 154301.

(12) Basu, S.; Francoeur, M. Near-field radiative transfer based thermal rectification using doped silicon. *Appl. Phys. Lett.* **2011**, *98*, 113106.

(13) Iizuka, H.; Fan, S. Rectification of evanescent heat transfer between dielectric-coated and uncoated silicon carbide plates. *J. Appl. Phys.* **2012**, *112*, 024304.

(14) Kou, J.; Minnich, A. J. Dynamic optical control of near-field radiative transfer. *Opt. Express* **2018**, *26*, A729–A736.

(15) Ben-Abdallah, P.; Biehs, S.-A. Near-Field Thermal Transistor. *Phys. Rev. Lett.* **2014**, *112*, 044301.

(16) Ito, K.; Nishikawa, K.; Iizuka, H.; Toshiyoshi, H. Experimental investigation of radiative thermal rectifier using vanadium dioxide. *Appl. Phys. Lett.* **2014**, *105*, 253503.

(17) Ito, K.; Nishikawa, K.; Miura, A.; Toshiyoshi, H.; Iizuka, H. Dynamic Modulation of Radiative Heat Transfer beyond the Blackbody Limit. *Nano Lett.* **2017**, *17*, 4347–4353.

(18) Fiorino, A.; Thompson, D.; Zhu, L.; Mittapally, R.; Biehs, S.-A.; Bezencenet, O.; El-Bondry, N.; Bansropun, S.; Ben-Abdallah, P.; Meyhofer, E.; Reddy, P. A Thermal Diode Based on Nanoscale Thermal Radiation. *ACS Nano* **2018**, *12*, 5774–5779.

(19) Wang, F.; Zhang, Y.; Tian, C.; Girit, C.; Zettl, A.; Crommie, M.; Shen, Y. R. Gate-Variable Optical Transitions in Graphene. *Science* **2008**, *320*, 206–209.

(20) Freitag, M.; Chiu, H.-Y.; Steiner, M.; Perebeinos, V.; Avouris, P. Thermal infrared emission from biased graphene. *Nat. Nanotechnol.* **2010**, *5*, 497–501.

(21) Ju, L.; Geng, B.; Horng, J.; Girit, C.; Martin, M.; Hao, Z.; Bechtel, H. A.; Liang, X.; Zettl, A.; Shen, Y. R.; Wang, F. Graphene plasmonics for tunable terahertz metamaterials. *Nat. Nanotechnol.* **2011**, *6*, 630–634.

(22) Fang, Z.; Thongrattanasiri, S.; Schlather, A.; Liu, Z.; Ma, L.; Wang, Y.; Ajayan, P. M.; Nordlander, P.; Halas, N. J.; Garcia de Abajo, F. J. Gated Tunability and Hybridization of Localized Plasmons in Nanostructured Graphene. *ACS Nano* **2013**, *7*, 2388–2395.

(23) Brar, V. W.; Sherrott, M. C.; Jang, M. S.; Kim, S.; Kim, L.; Choi, M.; Sweatlock, L. A.; Atwater, H. A. Electronic modulation of infrared radiation in graphene plasmonic resonators. *Nat. Commun.* **2015**, *6*, 7032.

(24) Sherrott, M. C.; Hon, P. W. C.; Fountaine, K. T.; Garcia, J. C.; Ponti, S. M.; Brar, V. W.; Sweatlock, L. A.; Atwater, H. A. Experimental Demonstration of > 230 Phase Modulation in Gate-Tunable Graphene-Gold Reconfigurable Mid-Infrared Metasurfaces. *Nano Lett.* **2017**, *17*, 3027–3034.

(25) Lee, J.; Wang, Z.; He, K.; Yang, R.; Shan, J.; Feng, P. X.-L. Electrically tunable single- and few-layer MoS₂ nanoelectromechanical systems with broad dynamic range. *Sci. Adv.* **2018**, *4*, No. ea06653.

(26) Shchegrov, A. V.; Joulain, K.; Carminati, R.; Greffet, J.-J. Near-Field Spectral Effects due to Electromagnetic Surface Excitations. *Phys. Rev. Lett.* **2000**, *85*, 1548–1551.

(27) Song, B.; Fiorino, A.; Meyhofer, E.; Reddy, P. Near-field radiative thermal transport: From theory to experiment. *AIP Adv.* **2015**, *5*, 053503.

(28) Hu, L.; Narayanaswamy, A.; Chen, X.; Chen, G. Near-field thermal radiation between two closely spaced glass plates exceeding Planck's blackbody radiation law. *Appl. Phys. Lett.* **2008**, *92*, 133106.

(29) Shen, S.; Narayanaswamy, A.; Chen, G. Surface Phonon Polaritons Mediated Energy Transfer between Nanoscale Gaps. *Nano Lett.* **2009**, *9*, 2909–2913.

(30) Narayanaswamy, A.; Shen, S.; Chen, G. Near-field radiative heat transfer between a sphere and a substrate. *Phys. Rev. B: Condens. Matter Mater. Phys.* **2008**, *78*, 115303.

(31) Lang, S.; Sharma, G.; Molesky, S.; Krnziem, P. U.; Jalas, T.; Jacob, Z.; Petrov, A. Y.; Eich, M. Dynamic measurement of near-field radiative heat transfer. *Sci. Rep.* **2017**, *7*, 13916.

(32) Song, B.; Thompson, D.; Fiorino, A.; Ganjeh, Y.; Reddy, P.; Meyhofer, E. Radiative heat conductances between dielectric and metallic parallel plates with nanoscale gaps. *Nat. Nanotechnol.* **2016**, *11*, 509–514.

(33) Watjen, J. I.; Zhao, B.; Zhang, Z. M. Near-field radiative heat transfer between doped-Si parallel plates separated by a spacing down to 200nm. *Appl. Phys. Lett.* **2016**, *109*, 203112.

(34) Kim, K.; Song, B.; Fernandez-Hurtado, V.; Lee, W.; Jeong, W.; Cui, L.; Thompson, D.; Feist, J.; Reid, M. T. H.; Garcia-Vidal, F. J.; Cuevas, J. C.; Meyhofer, E.; Reddy, P. Radiative heat transfer in the extreme near field. *Nature* **2015**, *528*, 387–391.

(35) Bernardi, M. P.; Milovich, D.; Francoeur, M. Radiative heat transfer exceeding the blackbody limit between macroscale planar surfaces separated by a nanosize vacuum gap. *Nat. Commun.* **2016**, *7*, 12900.

(36) Ito, K.; Miura, A.; Iizuka, H.; Toshiyoshi, H. Parallel-plate submicron gap formed by micromachined low-density pillars for near-field radiative heat transfer. *Appl. Phys. Lett.* **2015**, *106*, 083504.

(37) Song, B.; Ganjeh, Y.; Sadat, S.; Thompson, D.; Fiorino, A.; Fernandez-Hurtado, V.; Feist, J.; Garcia-Vidal, F. J.; Cuevas, J. C.; Reddy, P.; Meyhofer, E. Enhancement of near-field radiative heat transfer using polar dielectric thin films. *Nat. Nanotechnol.* **2015**, *10*, 253–258.

(38) Zhang, Z. M.; Basu, S. Entropy flow and generation in radiative transfer between surfaces. *Int. J. Heat Mass Transfer* **2007**, *50*, 702–712.

(39) Guo, Y.; Jacob, Z. Thermal hyperbolic metamaterials. *Opt. Express* **2013**, *21*, 15014–15019.

(40) Rodriguez, A. W.; Ilic, O.; Bermel, P.; Celanovic, I.; Joannopoulos, J. D.; Soljai, M.; Johnson, S. G. Frequency-Selective Near-Field Radiative Heat Transfer between Photonic Crystal Slabs: A Computational Approach for Arbitrary Geometries and Materials. *Phys. Rev. Lett.* **2011**, *107*, 114302.

(41) Basu, S.; Wang, L. Near-field radiative heat transfer between doped silicon nanowire arrays. *Appl. Phys. Lett.* **2013**, *102*, 053101.

(42) Joulain, K.; Drevillon, J.; Ben-Abdallah, P. Noncontact heat transfer between two metamaterials. *Phys. Rev. B: Condens. Matter Mater. Phys.* **2010**, *81*, 165119.

(43) Chen, K.; Santhanam, P.; Sandhu, S.; Zhu, L.; Fan, S. Heat-flux control and solid-state cooling by regulating chemical potential of photons in near-field electromagnetic heat transfer. *Phys. Rev. B: Condens. Matter Mater. Phys.* **2015**, *91*, 134301.

(44) Ding, D.; Kim, T.; Minnich, A. J. Active thermal extraction of near-field thermal radiation. *Phys. Rev. B: Condens. Matter Mater. Phys.* **2016**, *93*, 081402.

(45) Chiloyan, V.; Garg, J.; Esfarjani, K.; Chen, G. Transition from near-field thermal radiation to phonon heat conduction at sub-nanometre gaps. *Nat. Commun.* **2015**, *6*, 6755.

(46) Narayanaswamy, A.; Zheng, Y. A Green's function formalism of energy and momentum transfer in fluctuational electrodynamics. *J. Quant. Spectrosc. Radiat. Transfer* **2014**, *132*, 12–21.

(47) Ilic, O.; Jablan, M.; Joannopoulos, J. D.; Celanovic, I.; Buljan, H.; Soljai, M. Near-field thermal radiation transfer controlled by plasmons in graphene. *Phys. Rev. B: Condens. Matter Mater. Phys.* **2012**, *85*, 155422.

(48) Svetovoy, V. B.; van Zwol, P. J.; Chevrier, J. Plasmon enhanced near-field radiative heat transfer for graphene covered dielectrics. *Phys. Rev. B: Condens. Matter Mater. Phys.* **2012**, *85*, 155418.

(49) Ben-Abdallah, P.; Belarouci, A.; Frechette, L.; Biehs, S.-A. Heat flux splitter for near-field thermal radiation. *Appl. Phys. Lett.* **2015**, *107*, 053109.

(50) Ilic, O.; Thomas, N. H.; Christensen, T.; Sherrott, M. C.; Soljai, M.; Minnich, A. J.; Miller, O. D.; Atwater, H. A. Active Radiative Thermal Switching with Graphene Plasmon Resonators. *ACS Nano* **2018**, *12*, 2474.

(51) Messina, R.; Ben-Abdallah, P. Graphene-based photovoltaic cells for near-field thermal energy conversion. *Sci. Rep.* **2013**, *3*, 1383.

(52) Yang, J.; Du, W.; Su, Y.; Fu, Y.; Gong, S.; He, S.; Ma, Y. Observing of the super-Planckian near-field thermal radiation between graphene sheets. *Nat. Commun.* **2018**, *9*, 4033.

(53) van Zwol, P. J.; Thiele, S.; Berger, C.; de Heer, W. A.; Chevrier, J. Nanoscale Radiative Heat Flow due to Surface Plasmons in Graphene and Doped Silicon. *Phys. Rev. Lett.* **2012**, *109*, 264301.

(54) Papadakis, G. T.; Zhao, B.; Buddhiraju, S.; Fan, S. Gate-Tunable Near-Field Heat Transfer. *ACS Photonics* **2019**, *6*, 709–719.

(55) Rytov, S. M. *Theory of electric fluctuations and thermal radiation*; Air Force Cambridge Research Center: Bedford, MA, 1953.

(56) Polder, D.; Van Hove, M. Theory of Radiative Heat Transfer between Closely Spaced Bodies. *Phys. Rev. B* **1971**, *4*, 3303–3314.

(57) Rytov, S. M.; Kravtsov, Y. A.; Tatarskii, V. I. *Principles of Statistical Radiophysics*; Springer, 1987; Vol. 2, DOI DOI: 10.1007/978-3-642-69201-7.

(58) Brar, V. W.; Jang, M. S.; Sherrott, M.; Kim, S.; Lopez, J. J.; Kim, L. B.; Choi, M.; Atwater, H. Hybrid Surface-Phonon-Plasmon Polariton Modes in Graphene/Monolayer h-BN Heterostructures. *Nano Lett.* **2014**, *14*, 3876–3880.

(59) Dai, S.; Ma, Q.; Liu, M. K.; Andersen, T.; Fei, Z.; Goldflam, M. D.; Wagner, M.; Watanabe, K.; Taniguchi, T.; Thiemens, M.; Keilmann, F.; Janssen, G. C. a. M.; Zhu, S.-E.; Jarillo-Herrero, P.; Fogler, M. M.; Basov, D. Graphene on hexagonal boron nitride as a tunable hyperbolic metamaterial. *Nat. Nanotechnol.* **2015**, *10*, 682–686.

(60) Kitamura, R.; Pilon, L.; Jonasz, M. Optical constants of silica glass from extreme ultraviolet to far infrared at near room temperature. *Appl. Opt.* **2007**, *46*, 8118–8133.

(61) Biehs, S.-A.; Rousseau, E.; Greffet, J.-J. Mesoscopic Description of Radiative Heat Transfer at the Nanoscale. *Phys. Rev. Lett.* **2010**, *105*, 234301.

(62) Falkovsky, L. A. Optical properties of graphene. *J. Phys.: Conf. Ser.* **2008**, *129*, 012004.

(63) Lyon, T.; Sichau, J.; Dorn, A.; Centeno, A.; Pesquera, A.; Zurutuza, A.; Blick, R. Probing Electron Spin Resonance in Monolayer Graphene. *Phys. Rev. Lett.* **2017**, *119*, 066802.